A Wide Bandwidth GaN Switching Power Amplifier of Active Magnetic Bearing for a Flywheel Energy Storage System

Hong-Jin Hu, Kun Liu, Haoze Wang, *Member, IEEE*, and Jing-Bo Wei

***Abstract*— A switching power amplifier (SPA) provides the driving current for an active magnetic bearing (AMB) to achieve magnetic suspension (MS) control. The performances of the current bandwidth and current ripple should be significantly considered in the SPA of the AMB. The SPA can obtain a wide bandwidth by increasing the dc-link voltage. However, a high dc-link voltage will cause a high current ripple. To achieve a wide bandwidth and low current ripple, a new GaN-device-based SPA for the AMB of a flywheel energy storage system (FESS) is proposed in this article. The GaN SPA can operate at a high switching frequency and high dc-link voltage. Thus, the GaN SPA can improve the performance of the current bandwidth and current ripple compared to the conventional SPA. According to the characteristics of the GaN SPA, a low-loss PWM method and an optimal dead time strategy is proposed to increase the efficiency of the SPA. Furthermore, a high-response control approach of dead-beat model predictive control is proposed to further improve the current bandwidth. The proposed GaN SPA is applied in a 500-kW MS FESS prototype. The effectiveness of the SPA is verified experimentally.**

***Index Terms*—Active magnetic bearing (AMB), flywheel energy storage system (FESS), GaN device, switching power amplifier (SPA).**

I. INTRODUCTION

ENERGY storage systems (ESSs) play an increasingly significant role in industrial applications. Among the variety of ESSs, flywheel energy storage systems (FESSs) have several advantages, including fast response, high instantaneous power, high efficiency, low maintenance, and long lifetime [1], [2], [3]. As a result, FESSs have been utilized in many applications, such as electric vehicles [4], [5], railways [6], wind generators [7], [8], photovoltaic systems [9], microgrids [10], UPS systems [11], [12], and aerospace systems [13], [14]. In FESSs, the energy is stored in a high rotation speed flywheel rotor. The flywheel rotor is generally suspended by an active magnetic bearing (AMB) system to achieve a high rotation speed without friction. The AMB should be driven by a power amplifier (PA) to generate a suspension force. Based on the literature, the performances of the current bandwidth and current ripple of the PA should be significantly considered [15], [16]. One reason for the need for a wide bandwidth is that the flywheel rotor will suffer from a high-frequency exciting force caused by the rotor eccentric mass. The PA should have the ability to generate a high-frequency current to overcome the exciting force. Additionally, increasing the current bandwidth is an effective way to overcome the whirl motion of the flywheel rotor and enhance the stability of the AMB control system. The PA in the AMB also requires a low current ripple, because the current ripple causes a force ripple, which reduces the control accuracy.

The PA in the AMB can be divided into the linear power amplifier (LPA) and the switching power amplifier (SPA) [17], [18]. Compared to the SPA, the LPA has a poor performance in terms of volume and efficiency. Thus, the SPA is most commonly used in AMBs, and PA research is almost entirely focused on the SPA. To increase the bandwidth of the SPA, many methods have been proposed in recent years. One of the major ways to broaden the bandwidth is to increase the dc-link voltage of the SPA. In [19], the relationships among bandwidth, current ripple, dc-link voltage, coil resistance, and coil inductance were analyzed. The SPA can obtain a wider current bandwidth and a faster current response by increasing the dc-link voltage. However, increasing the dc-link voltage will cause a large current ripple. The current ripple will cause a magnetic force ripple and vibration to the flywheel rotor. To suppress the current ripple, a current-mode three-level PWM SPA was proposed in [20]. The current ripple can also be reduced by increasing the switching frequency. However, the general Si-base SPA of the AMB is generally limited to a switching frequency of 20 kHz. Applying a wide band gap (WBG) device can broaden the switching frequency. In [15] and [21], the WBG device SiC MOSFET was utilized in the SPA. The SPA can achieve a high dc-link voltage and high switching frequency by using the WBG device. The utilization of WBG devices in the SPA is a promising approach to achieve a wide bandwidth and low current ripple.

Increasing the dc-link voltage is an efficient way to broaden the bandwidth. However, the dc-link voltage is limited by electrical insulation. While maintaining the same dc-link voltage, the

Manuscript received 17 May 2022; revised 7 August 2022; accepted 21 September 2022. Date of publication 28 September 2022; date of current version 18 November 2022. This work was supported by Shenzhen Science and Technology Program under Grant JCYJ20200109142205924 and Grant 202001093000459. Recommended for publication by Associate Editor M. Hartmann. *(Corresponding author: Jing-Bo Wei.)*

The authors are with the School of Aeronautics and Astronautics, Sun Yat-Sen University, Shenzhen 518107, China (e-mail: hongjinhu@foxmail.com; liukun6@mail.sysu.edu.cn; wanghz5@mail.sysu.edu.cn; weijb5@mail.sysu.edu.cn).

Color versions of one or more figures in this article are available at https://doi.org/10.1109/TPEL.2022.3210249.

Digital Object Identifier 10.1109/TPEL.2022.3210249

bandwidth can be further increased by implementing a suitable current control method. In [22], an adaptive gain control method was proposed for the SPA of the AMB to increase the response speed, reduce the static error, and reduce the current ripple. In [23], an improved current control strategy with model prediction was proposed to achieve a fast response and wide bandwidth. Model predictive control (MPC) is regarded as a high-response control method. Several MPCs have been applied in the SPA to increase the bandwidth and response speed. In [24], a model predictive current control (MPCC) was used in the SPA to compensate for the time delay, which can increase the bandwidth and reduce the control error. In [25], a finite control set MPCC was proposed for the Wheatstone-bridge-winding AMB to increase the current bandwidth. The finite-control-set model predictive current control (FCSMPCC) can directly obtain the switching state without the requirement of the PWM module, which shows a concise control structure. In [26], the FCSMPCC was proposed for the five-phase six-leg SPA to achieve a high dynamic response and low steady-state error. From the literature, the MPCC shows several superior performances in the SPA, including a wide bandwidth, high response, and high accuracy. The MPCC is a promising control method for the current control for the SPA.

Increasing the dc-link voltage and switching frequency is an efficient way to obtain a wide bandwidth and low current ripple. Currently, most SPAs are developed by Si-based devices. The switching frequency of the Si-based SPA is generally limited to 20 kHz. Several SPAs developed by SiC MOSFET were proposed in [15] and [21]. The switching frequency can be broadened to 50 kHz. However, the switching frequency is relatively low compared to state-of-the-art power electronic devices. It is reported that the GaN HEMT can be operated at a high switching frequency, which can be larger than 100 kHz [27], [29]. Applying the GaN HEMT to the SPA of the AMB can further promote the SPA performance. Nevertheless, the GaN HEMT shows some unique characteristics compared to conventional devices, which should be considered in the SPA application. The GaN HEMT does not have an antiparallel diode. When reverse conduction occurs and there is no gate driving signal, the GaN HEMT exhibits diode-like behavior. This diode-like behavior causes a large voltage drop and reverses conduction loss [28], [29]. Thus, the time that occurs diode-like behavior should be minimized in the GaN HEMT [30]. In recent years, the dead time optimization strategies for GaN-based converters were proposed to reduce reverse conduction loss [30], [34]. The optimal dead time (OTD) can be obtained through the experimental test [31], [32]. In this way, the OTD is accurate and reliable. However, this way is not scalable because it depends on the parameters of the circuit. When the parameters of the circuit are changed, a new experimental test is required, which is labor-consuming. To avoid numerous experiments, the OTD strategies based on a theoretical switching model were proposed in [30], [33], and [34]. These theoretical OTD strategies have been applied to synchronous buck converter [30], clamp flyback converter [33], and boost converter [34].

H-bridge circuit topology is a commonly used topology in the SPA [15], [24], and [35]. The H-bridge generally needs a PWM method to regulate output voltage for current control. In the SPA, the PWM method can be classified into two-level and three-level modulation methods [15] and [20]. In the two-level PWM method, the PWM signal applies to devices of different bridge arm operates, which will not cause a shoot-through and have high reliability. However, the two-level PWM requires a diode freewheeling state. In the diode freewheeling state, GaN HEMT exhibits diode-like behavior and has a large reverse conduction loss. In the three-level PWM method, the devices of the bridge arm require the complementary PWM signal, which is similar to the synchronization rectifier mode of the dc/dc converter [36] and [37]. The H-bridge circuit with the three-level PWM method can avoid the diode freewheeling state. However, all the device in the H-bridge needs a PWM signal, which will cause a high switching time and switching loss. Considering the characteristics of the GaN HEMT, a PWM method that can avoid diode freewheeling state and reduce switching times is appreciated in GaN SPA.

In this article, a new GaN SPA is proposed for the AMB. The GaN SPA can operate at a high voltage and high switching frequency. Thus, the GaN SPA can achieve a wide bandwidth and low current ripple. The high switching frequency causes high switching loss. To reduce the switching loss, a low-loss PWM method is proposed for the GaN SPA. Considering the diode-like behavior, an ODT strategy is proposed for reducing the time duration of diode-like behavior and increasing the efficiency of the SPA. To further improve the current bandwidth, a dead-beat MPCC (DBMPCC) is proposed for the GaN SPA. The novelty and contribution of this article are presented as follows.

1) A new GaN SPA is proposed for the AMB of the FESS to achieve wide bandwidth and low current ripple. Considering the characteristics of the GaN SPA, the corresponding low-loss PWM method, ODT strategy, and DBMPCC are proposed.
2) An experimental comparison of the proposed GaN SPA and existing SPA is reported. A comparison of the proposed low-loss PWM method and the existing two-level and three-level PWM methods is presented. A comparison of the proposed DBMPCC, conventional PID control, and existing FCSMPCC is performed.
3) The implementation of the GaN SPA in a five-degree of freedom (5-DOF) magnetic suspension (MS) control system is reported.

The remainder of this article is organized as follows. In Section II, the configuration of AMBs in FEES is presented. In Section III, the wide bandwidth GaN SPA is proposed. The topology of the GaN SPA, the low-loss PWM method, and the ODT strategy are presented. In Section IV, DBMPCC is proposed for the GaN SPA, and the stability of the DBMPCC is analyzed. In Section V, an experiment with the proposed GaN SPA is performed on a 500-kW MS FESS prototype. Finally, the conclusions are drawn in Section VI.

II. CONFIGURATION OF AMBS IN FESS

An FESS is a type of mechanical energy storage device in which the mechanical energy is stored in a high rotation speed

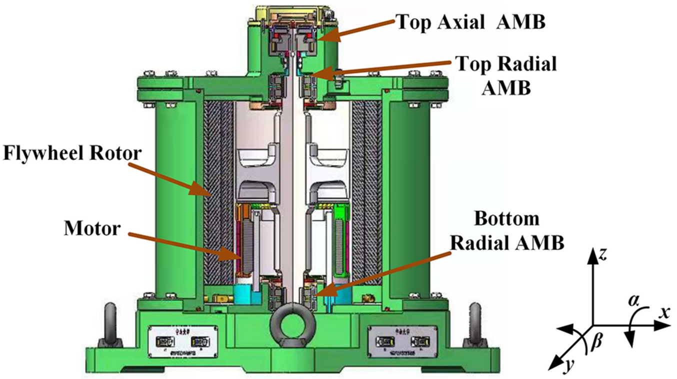

Fig. 1. Configuration of AMBs in the FESS.

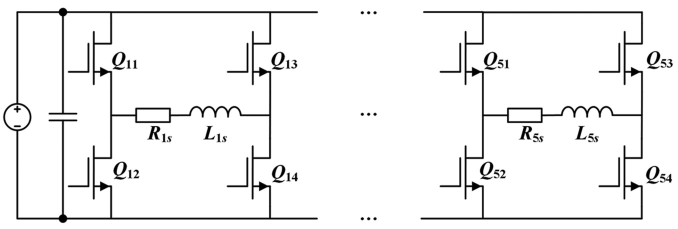

Fig. 2. Topology of the proposed GaN SPA.

flywheel rotor. The AMBs are utilized in the FESS to suspend the flywheel rotor, which can achieve a high rotation speed without friction. The configuration of the AMBs in the FESS is shown in Fig. 1. The FESS has three AMBs: the top radial AMB, bottom radial AMB, and top axial AMB. The radial AMB has two excitation coils, and the axial AMB has one excitation coil. Thus, the SPA should generate five-channel currents to the AMBs of the FESS. By applying the appropriate current, the AMB system can achieve 5-DOF MS control of the flywheel rotor. The 5-DOF include the displacements of *x*, *y*, and *z* and the rotation angles of α and β. The current of the AMB is generated by the SPA. Thus, the performance of the SPA has a significant influence on the MS control.

III. PROPOSED WIDE BANDWIDTH GAN SPA

In this section, the GaN SPA is proposed to achieve a wide current bandwidth and low current ripple. For the proposed GaN SPA, the topology of the GaN SPA, low-loss PWM method, and ODT strategy are presented.

A. Topology of the SPA

The SPA of the AMB generally uses a circuit topology of an H-bridge. The SPA needs to generate a five-channel current to achieve the 5-DOF MS control. Thus, the proposed GaN SPA should include five H-bridges, which are presented in Fig. 2. The GaN HEMT in the SPA needs to employ a gate driver to achieve turn on or turn off. The gate driver circuit of the GaN SPA is shown in Fig. 3. The drive circuit requires a suitable turn-on and turn-off resistor. An excessive small turn-ON and turn-OFF resistor will cause a switching oscillation and electromagnetic interference. An excessive large turn-ON and turn-OFF resistor will cause long turn-ON and turn-OFF time and significant switching loss. In Fig. 3, the turn-ON and turn-OFF resistor is presented as

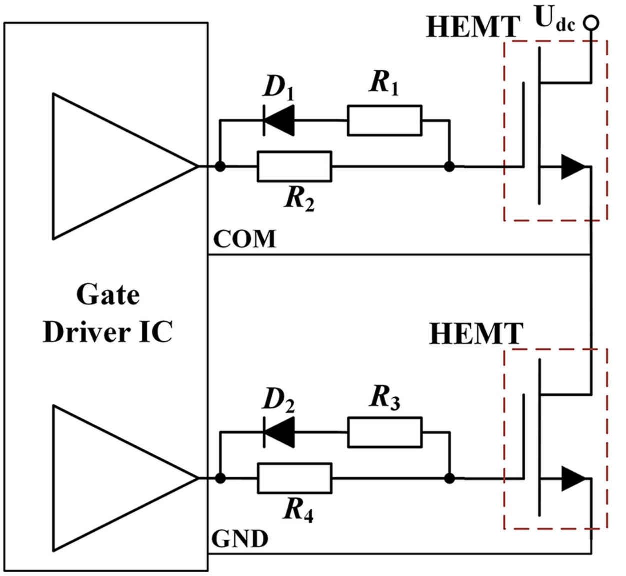

Fig. 3. Gate driver circuit of the GaN SPA.

$$R_{\text{on}} = R_2 = R_4 \text{ and } R_{\text{off}} = \frac{R_1 R_2}{R_1 + R_2} = \frac{R_3 R_4}{R_3 + R_4} \tag{1}$$

where R_{on} is the turn-on resistor and R_{off} is the turn-off resistor.

The five H-bridges of the SPA operate independently. The excitation coil connected to the H-bridge is equivalent to a resistance inductance series. Thus, the relationship between the coil voltage and coil current can be deduced as

$$\frac{di_c}{dt} = -\frac{R}{L} i_c + \frac{1}{L} u_c \tag{2}$$

where i_c is the coil current, u_c is the coil voltage, *R* is the coil resistor, and *L* is the coil inductance.

According to (1), the coil current i_c can be controlled by controlling the voltage u_c. The voltage u_c can be generated by applying an appropriate PWM method.

B. Low-Loss PWM Method

A suitable PWM method should be applied to the GaN SPA to achieve current control. The switching frequency of the GaN SPA is high, which will cause a high switching loss. In this article, a low-loss PWM method is proposed to reduce switching times. With the proposed PWM method, the two bridge arms of the SPA operate separately. At the same moment, only one bridge arm applied the PWM signal. By judging the voltage sign, one bridge arm generates a positive voltage for the coil, and the other generates a negative voltage for the coil. Thus, the switching times of the SPA can be reduced.

When GaN SPA generates a positive voltage, the PWM signals are shown in Fig. 4. The GaN device Q_{n4} is kept in the ON state. The PWM signals are applied to Q_{n1} and Q_{n2}. At time t_1, Q_{n1} is

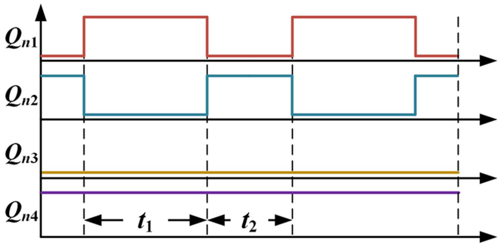

Fig. 4. PWM signals with positive voltage.

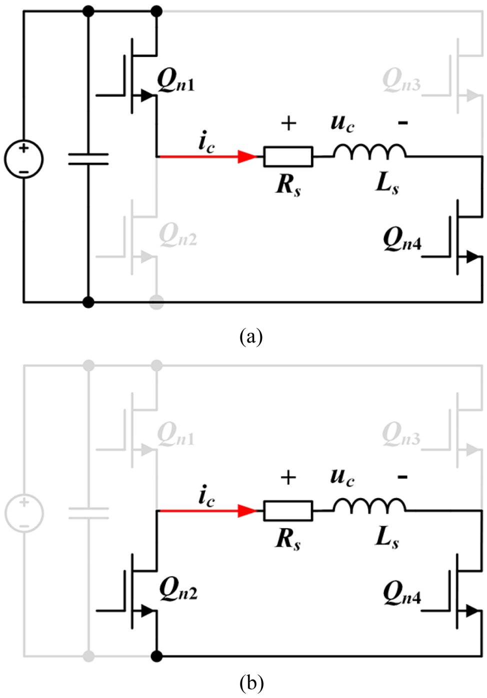

(a)

(b)

Fig. 5. SPA generates positive voltage. (a) Q_{n1} is ON and Q_{n2} is OFF. (b) Q_{n1} is OFF and Q_{n2} is ON.

ON and Q_{n2} is OFF, which is shown in Fig. 5(a). The coil voltage is equal to the dc-link voltage. At time t_2, Q_{n1} is OFF and Q_{n2} is ON, which is shown in Fig. 5(b). The coil voltage is equal to zero. When the current is positive at time t_2, Q_{n2} operates in the state of reverse conduction and has a gate driving signal. Thus, the GaN HEMT in the SPA can prevent diode-like behavior and achieve low reverse conduction loss. The relationship between the average output voltage and the duty cycle can be deduced as

$$u_c = \frac{U_{\text{dc}} t_1}{t_1 + t_2} = D_T U_{\text{dc}} \tag{3}$$

where U_{dc} is the dc-link voltage and D_T is the duty cycle of the PWM signal.

When the GaN SPA generates a negative voltage, the PWM signals are shown in Fig. 6. The GaN device Q_{n2} is kept in the ON state. The PWM signals are applied to Q_{n3} and Q_{n4}. At time t_3, Q_{n3} is ON and Q_{n4} is OFF, as shown in Fig. 7(a). The coil voltage is equal to the negative dc-link voltage. At time t_4, Q_{n3} is OFF and Q_{n4} is ON, which is shown in Fig. 7(b). The coil voltage is equal to zero. The relationship between the average

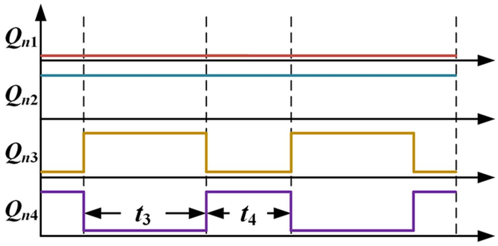

Fig. 6. PWM signals with negative voltage.

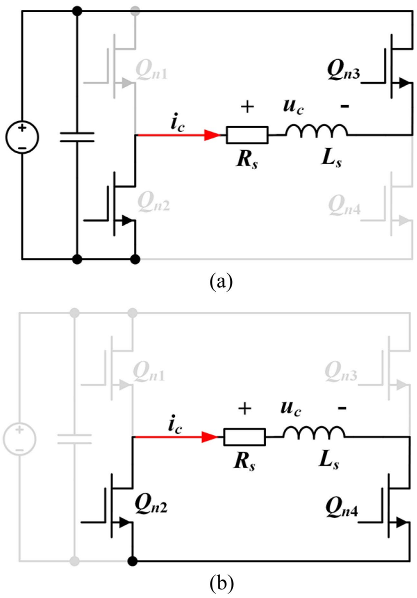

(a)

(b)

Fig. 7. SPA generates negative voltage. (a) Q_{n3} is ON and Q_{n4} is OFF. (b) Q_{n3} is OFF and Q_{n4} is ON.

voltage and the PWM duty cycle is presented as

$$u_c = -\frac{U_{\text{dc}} t_3}{t_3 + t_4} = -D_T U_{\text{dc}}. \tag{4}$$

According to (3) and (4), the output voltage of the SPA is proportional to the duty cycle. The output voltage can be regulated by the duty cycle.

In the three-level PWM method, four devices of the H-bridge should apply PWM signals [20]. Compared to the three-level PWM method, the switching times of the proposed PWM method can be reduced by half. Two-level PWM has low switching times [15]. However, the two-level PWM requires a diode freewheeling state. In the diode freewheeling state, GaN HEMT exhibits diode-like behavior, which causes a large reverse conduction loss. The GaN SPA with the two-level PWM method will have low efficiency. Compared to the three-level PWM method and two-level PWM method, the proposed PWM method can result in a lower loss in the GaN SPA.

C. ODT Strategy

The PWM signals in Figs. 4 and 6 are the ideal signals.

In practice, the GaN HMET has a turn-ON time and turn-OFF time. Considering the turn-ON time and turn-OFF time,

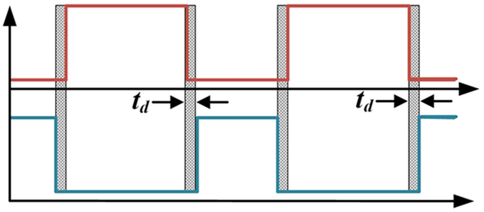

Fig. 8. PWM signals with dead time.

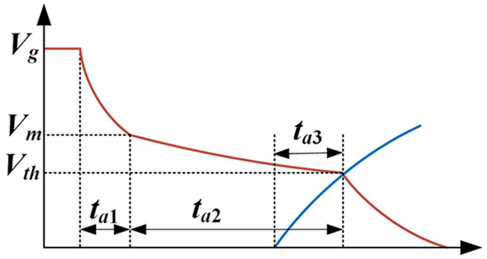

Fig. 9. Optimal switching process of Q_{n1} and Q_{n2}.

the gate PWM signals need a dead-time interval to prevent shoot-through. The PWM signals with dead-time intervals are presented in Fig. 8. The dead-time interval in the GaN SPA cannot be excessively long because GaN will exhibit diode-like behavior during the dead-time interval. A long dead-time interval causes a large reverse conduction loss. Thus, the GaN SPA requires an OTD that can prevent shoot-through and minimize reverse conduction loss.

The optimal switching process for the turn-ON and turn-OFF processes of Q_{n1} and Q_{n2} is shown in Fig. 9. The gate voltage of Q_{n1} drops down to the threshold voltage $V_{th,}$ and the gate voltage of Q_{n2} rises up to V_{th}. In this process, the dead time is the minimized dead time that prevents shoot-through.

As shown in Fig. 9, the turn-OFF process can be divided into three stages. In the first stage, the gate voltage drops from V_g to the Miller voltage V_m. In the second stage, the gate voltage drops from V_m to V_{th}. In the third stage, the gate voltage drops from V_{th} to zero.

The Miller voltage can be obtained from [38], which is presented as

$$V_m = V_{\text{th}} + \frac{i_c}{g_m} \tag{5}$$

where g_m is the transconductance.

The transconductance g_m depends on the drain current I_{ds}. However, the relationship between the current I_{ds} and transconductance g_m is nonlinear. Thus, it is difficult to find the exact value of the Miller voltage V_m using (5).

A good approximation is to find the average transconductance g_m from the current I_{ds} versus the gate-to-source voltage V_{gs} characteristic curve of the device datasheet [39]. The g_m is presented as

$$g_m = \frac{\Delta I_{ds}}{\Delta V_{gs}}. \tag{6}$$

By obtaining the Miller voltage, the duration of the first stage t_{a1} can be calculated as

$$t_{a1} = R_{\text{off}} C_{gs} \ln\left(\frac{V_g}{V_m}\right) \tag{7}$$

where C_{gs} is the gate-to-source capacitance.

In the second stage, C_{gs} and C_{gd} show nonlinearity during the Miller platform. Thus, the duration calculated by using the capacitance model is very complex. The utilization of equivalent capacitance is an efficient way to calculate the time interval that the gate voltage deduces from V_m to V_{th} [30].

In the overall turn-OFF processes, the relationship among the gate charge quantities is presented as

$$Q_g = Q_{a1} + Q_m + Q_{\text{th}} \tag{8}$$

where Q_g is the charge of the overall turn-off processes, Q_{a1} is the charge of the first stage, Q_{th} is the charge of the third stage, and Q_m is the charge of the Miler platform process.

The charges of Q_{th} and Q_g can be obtained from the device datasheet. Q_{a1} can be deduced as

$$Q_{a1} = C_{gs}\left(V_g - V_m\right). \tag{9}$$

From (8) and (9), the equivalent capacitance of the second stage can be deduced as

$$C_{\text{eq}} = \frac{Q_g - C_{gs}V_g + C_{gs}V_m - Q_{\text{th}}}{(V_m - V_{\text{th}})}. \tag{10}$$

Thus, the time interval t_{a2} can be deduced as

$$t_{a2} = R_{\text{off}} \frac{Q_g - C_{gs}V_g + C_{gs}V_m - Q_{\text{th}}}{(V_m - V_{\text{th}})} \ln\left(\frac{V_m}{V_{\text{th}}}\right). \tag{11}$$

The time interval at which the gate voltage rises from 0 to V_{th}, i.e., t_{a3}, is deduced as

$$t_{a3} = -R_{\text{on}} C_{gs} \ln\left(\frac{V_g - V_{\text{th}}}{V_g}\right). \tag{12}$$

Combining (7), (11), and (12), the OTD can be deduced as

$$\begin{aligned} t_{od} = {} & R_{\text{off}} C_{gs} \ln\left(\frac{V_g}{V_m}\right) + R_{\text{off}} \frac{Q_g - C_{gs}V_g + C_{gs}V_m - Q_{\text{th}}}{(V_m - V_{\text{th}})} \\ & \times \ln\left(\frac{V_m}{V_{\text{th}}}\right) + R_{\text{on}} C_{gs} \ln\left(\frac{V_g - V_{\text{th}}}{V_g}\right). \end{aligned} \tag{13}$$

The dead time of (13) is a theoretical OTD. The dead time needs some margin in practical engineering. In practical engineering, the practical value is usually 1.2−1.4 times the design value to obtain a reasonable margin. Thus, the dead time applied to the GaN SPA is presented as

$$t_{pd} = (1 + \lambda)\, t_{od} \tag{14}$$

where t_{pd} is the practical dead time for the SPA, and λ ranges from 0.2 to 0.4.

IV. PROPOSED DBMPCC

The GaN SPA needs an appropriate control method to achieve current control. The MPCC is an efficient control method for the system to achieve a fast response. The MPCC can be mainly divided into two categories [26], [41], and [42], which is FC-SMPCC and continuous-control-set model predictive current control (CCSMPCC). The FCSMPCC does not need a PWM module and has a concise control structure [26]. However, the FCSMPCC only has a single switching state in one control period, and its switching frequency is generally not fixed, which will cause a high current ripple [41]. The CCSMPCC can have a lower current ripple than the FCSMPCC because the power converter can obtain multiple switching states in one control period. The DBMPCC is regarded fast response control approach, which has been widely applied to machine drives and grid-connected converters [41], [42], [43]. Thus, the GaN SPA adopts DBMPCC to improve the current bandwidth further. Additionally, to obtain a low current ripple, the DBMPCC is based on the framework of CCSMPCC.

A. Control Law Design

According to (2), the discrete current model of the SPA can be deduced as

$$i\left(k+1\right)=K_1 i\left(k\right)+K_2 u_c\left(k\right) \tag{15}$$

where

$$K_1=1-\frac{RT_s}{L},\ \text{and}\ K_2=\frac{T_s}{L}. \tag{16}$$

For the DBMPCC, the predictive current at the time of k+2 needs to the obtained according to the measured current at the time of k. According to (15), the predictive current at the time of k+2 can be deduced as

$$i_p\left(k+2\right)=K_1^2 i\left(k\right)+K_1K_2u_c\left(k\right)+K_2u_c\left(k+1\right) \tag{17}$$

where $i_p(k+2)$ is the predictive current at the time of k+2.

Parametric uncertainty causes errors in the predictive current model. To improve the accuracy of the predictive current model, feedback correction is utilized. In this article, the error between the predictive current and measured current is used to achieve feedback correction, which is presented as

$$\hat{i}_p\left(k+2\right)=i_p\left(k+2\right)+f\left(i\left(k\right)-\hat{i}_p\left(k\right)\right) \tag{18}$$

where f is the feedback correction coefficient.

The DBMPCC should make the predictive current reach the reference current. The control error is presented as

$$\begin{aligned}e\left(k+2\right)=&\ i_r-K_1^2 i\left(k\right)-K_1K_2u_c\left(k\right)\\&-K_2u_c\left(k+1\right)-f\left(i\left(k\right)-\hat{i}_p\left(k\right)\right).\end{aligned} \tag{19}$$

The control error of (17) should be zero. Thus, the control law can be deduced as

$$\begin{aligned}u_c\left(k+1\right)=&\ \frac{1}{K_2}i_r-\frac{K_1^2}{K_2}i\left(k\right)-K_1u_c\left(k\right)\\&-\frac{f}{K_2}\left(i\left(k\right)-i_p\left(k\right)\right).\end{aligned} \tag{20}$$

According to (20), the control law of the DBMPCC can be obtained by measuring the coil current. However, the control output of the SPA is limited in practice. The above DBMPCC does not consider the output saturation. Thus, a DBMPCC with considering output saturation (COS) is further deduced.

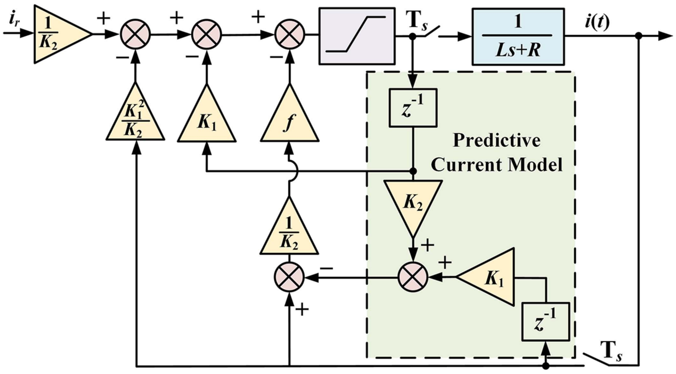

Fig. 10. Block diagram of the DBMPCC.

When output saturation occurs, the control error of (20) cannot reach zero. In this case, the designed control law should minimize the control error. The minimization problem of control error is presented as

$$\begin{aligned}&\min\left|e\left(k+2\right)\right|\\&\text{s.t.}\quad u_{\text{min}}\le u_{cs}\left(k+1\right)\le u_{\text{max}}\end{aligned} \tag{21}$$

where $u_{\min}$ is the minimum control output, $u_{\max}$ is the maximum control output, and u_{cs} is the control law with COS.

To solve the minimization problem, a function of $h(u_{cs}(k+1))$ is defined as

$$\begin{aligned}h\left(u_{cs}\left(k+1\right)\right)=&\left|e\left(k+2\right)\right|=\Big|i_r-K_1^2 i\left(k\right)-K_1K_2u_{cs}\left(k\right)\\&-K_2u_{cs}\left(k+1\right)-f\left(i\left(k\right)-\hat{i}_p\left(k\right)\right)\Big|.\end{aligned} \tag{22}$$

When $u(k+1) > u_{\max}$, output saturation occurs. According to (19) and (20), $h(u_{\max}) > 0$. K_1 and K_2 are larger than zero. Therefore, the inequality relation of (23) can be obtained

$$h\left(u_{\text{min}}\right)<h\left(u_{\text{max}}-\Delta u\right) \tag{23}$$

where Δu is a value large than zero.

According to (23), the control error $e(k+1)$ is minimized when $u_s = u_{\max}$.

Similarly, when the negative saturation occurs, u_{cs} should be equal to $u_{\min}$. Thus, the control law of the DBMPCC with COS is presented as

$$u_{cs}=\begin{cases}u_c\left(k+1\right), & u_{\text{min}}<u_c\left(k+1\right)<u_{\text{max}}\\u_{\text{max}}, & u_c\left(k+1\right)\ge u_{\text{max}}\\u_{\text{min}}, & u_c\left(k+1\right)\le u_{\text{min}}\end{cases}. \tag{24}$$

According to (20) and (24), the designed control law of the DBMPCC with COS is obtained. The control block diagram of the proposed DBMPCC is shown in Fig. 10. The control law calculation is almost multiplied and accumulated calculation, which is easy for the MCU to implement.

B. Stability Analysis

According to the theory of the DBMPCC, the output current can reach the reference in a finite beat, and the stability of the system can be ensured. However, the predictive model is different from the actual model. Thus, the stability analysis considering the model error is significant.

The control law of (20) is deduced as *z* transform form, which is presented as

$$zU_c(z) = \frac{1}{K_2} I_r(z) - \frac{K_1^2}{K_2} I(z) - K_1 U_c(z) - \frac{f}{K_2}\left(I(z) - I_p(z)\right). \tag{25}$$

The *z* transform form of the predictive model is presented as

$$zI_p(z) = K_1 I(z) + K_2 U_c(z). \tag{26}$$

Substituting (26) into (25), the control law can be further deduced as

$$U_c(z) = \frac{zI_r(z) + \left(\left(-f - K_1^2\right)z + K_1 f\right) I(z)}{K_2\left(z^2 + K_1 z - f\right)}. \tag{27}$$

The actual current model is presented as

$$zI(z) = K_{1r} I(z) + K_{2r} U(z). \tag{28}$$

K_{1r} and K_{2r} in (28) are presented as

$$K_{1a} = 1 - \frac{R_a T_s}{L_a}, \text{ and } K_{2a} = \frac{T_s}{L_a} \tag{29}$$

where R_a is the actual resistance, and L_a is the actual inductance.

Substituting (28) into (27), the closed-loop transfer function is deduced as

$$\frac{I(z)}{I_r(z)} = \frac{b_1 z}{a_3 z^3 + a_1 z^2 + a_1 z + a_0} \tag{30}$$

where

$$\begin{aligned} b_1 &= K_{2a} \\ a_3 &= K_2 \\ a_2 &= \left(K_1 K_2 - K_{1a} K_2\right) \\ a_1 &= \left(K_{2a} K_1^2 + f K_{2a} - K_{1a} K_2 K_1 - f K_2\right) \\ a_0 &= K_{1a} K_2 f - K_{2a} K_1 f. \end{aligned} \tag{31}$$

The error of resistance and inductance in the predictive model is presented as

$$\Delta R = \frac{R_a - R}{R_a} \text{ and } \Delta L = \frac{L_a - L}{L_a}. \tag{32}$$

Based on (30), the root locus of the deference between resistance and inductance is shown in Fig. 11. According to Fig. 11, the eigenvalue of the discrete system is zero when a model error is zero. When the model error occurs, the system can maintain stability within a certain model error range. With the model error increasing, the root locus will be outside the unit circle, and the system will be unstable.

When output saturation occurs, the control output is the maximum allowable output, and the system is an open-loop system.

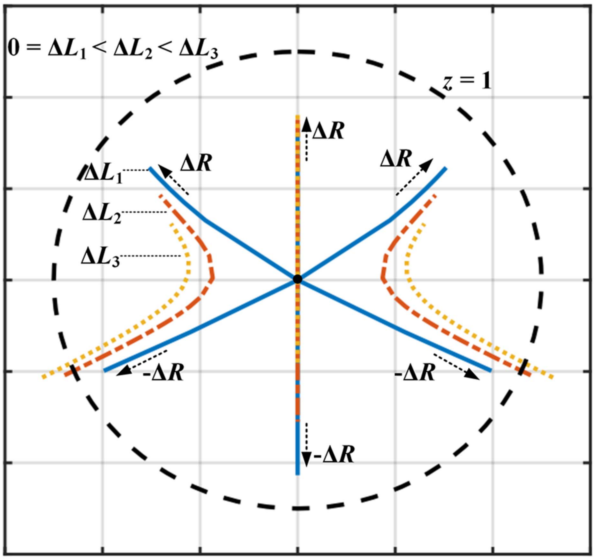

Fig. 11. Root locus of model error.

According to (15), the eigenvalue of the open-loop system is within the unit circle. Thus, the system is stable when output saturation occurs.

The feedback correction coefficient *f* will influence the control accuracy and stability. The steady-state error of the DBMPCC can be deduced as

$$e_s = \underset{z \to 1}{Lim}\left(1 - \frac{I(z)}{I_r(z)}\right) = 1 - \frac{b_1}{a_3 + a_1 + a_1 + a_0} \tag{33}$$

where e_s is the steady-state error.

According to (33), the steady-state error versus model error and feedback correction coefficient are shown in Fig. 12. The root locus of the feedback correction coefficient is shown in Fig. 13. From Fig. 12, choosing a larger feedback correction coefficient can achieve better control accuracy. Nevertheless, according to Fig. 13, a large feedback correction coefficient will cause degenerated stability. The feedback correction coefficient *f* can be determined according to the experimental test.

The above stability analysis illustrates that the proposed DBMPCC can ensure system stability within a certain range of model error.

V. EXPERIMENTAL RESULTS

The proposed GaN SPA is implemented in a 500 kW FESS prototype. To verify the effectiveness of the GaN SPA, the current bandwidth and current ripple of the GaN SPA are measured, and the experimental comparisons with the Si MOSFET SPA and SiC MOSFET SPA are presented. The DBMPCC is implemented in the GaN SPA to further improve the current bandwidth. To verify that the low-loss PWM method and the ODT strategy can improve the efficiency of the GaN SPA, the experimental comparisons with the conventional two-level PWM method [15] and three-level PWM method [20] are performed. Additionally, the GaN SPA is implemented in a 5-DOF AMB control system, and the control performance is presented.

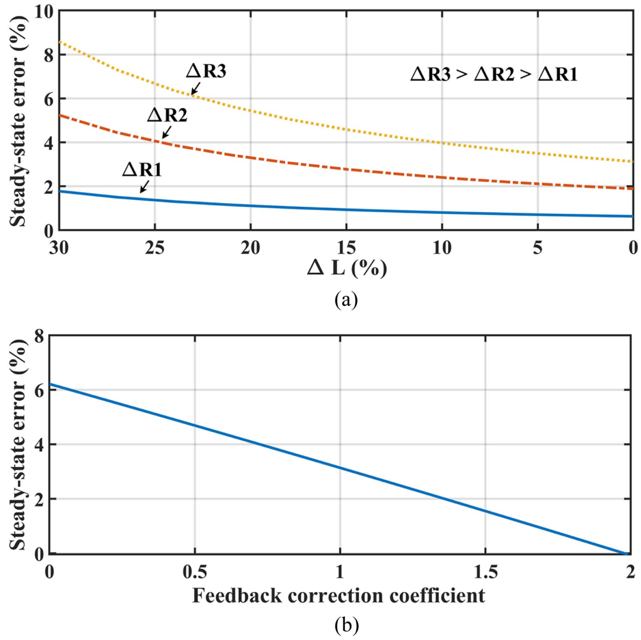

Fig. 12. (a) Steady-state error versus model error. (b) Steady-state error versus feedback correction coefficient.

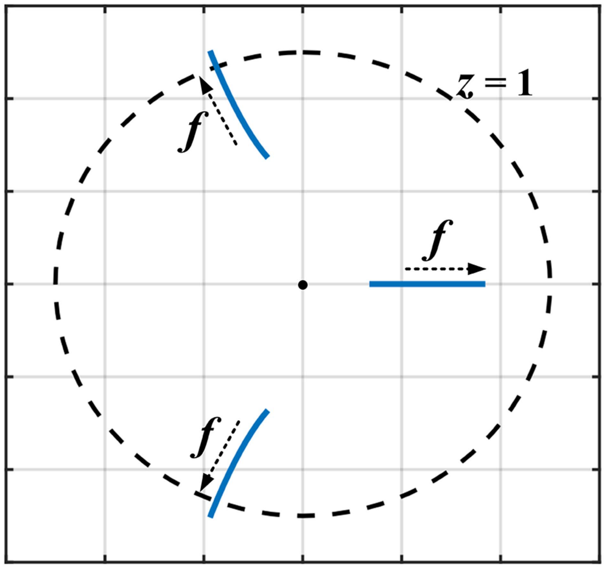

Fig. 13. Root locus of feedback correction coefficient.

A. Experimental Setup

The experimental platform is shown in Fig. 14. The experimental platform mainly includes the GaN SPA, MS FESS, spectrum analyzer, power analyzer, and oscilloscope. The GaN SPA is presented in Fig. 15(a). It mainly includes the XG65T125HS1B GaN HEMTs, IRS2110 gate drivers, and LA-25-NP current sensors. The controller of the SPA adopts a digital signal processor (DSP) and field-programmable gate array (FPAG) architecture, which is presented in Fig. 15(b). The DSP adopts TMS320C6713B, and the FPGA adopts XC3S1000.

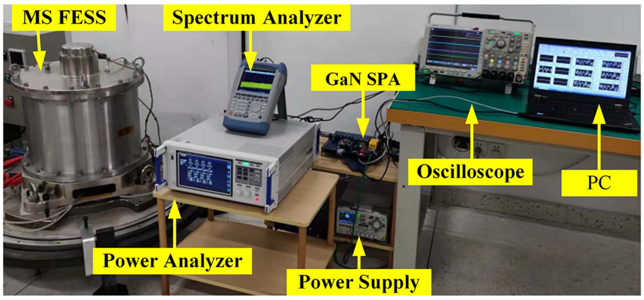

Fig. 14. Experimental platform of the 500 kW FESS prototype.

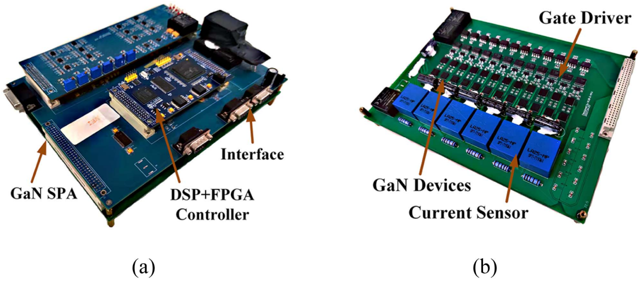

Fig. 15. (a) GaN SPA (b) GaN SPA with the DSP + FPAG controller.

TABLE I
MAIN PARAMETER SPECIFICATIONS OF THE GAN SPA

Symbol	Description	Value
V_{dc}	Maximum DC-link voltage	100 V
I_{dc}	Maximum current of one channel	3.6 A
f_{sw}	Switched frequency	120 kHz
fs	Sampling frequency	20 kHz
e_r	Accuracy of current sensor	0.5 %

TABLE II
MAIN PARAMETER SPECIFICATIONS OF THE GAN HEMT

Symbol	Description	Value
R_{on}	Turn-on resistor	18 Ω
R_{off}	Turn-off resistor	15 Ω
V_g	Gate drive voltage	12 V
Q_g	Total charge of turn-off process	18.7 nC
V_{th}	Threshold voltage	1.82 V
Q_{th}	Charge of threshold voltage	2.1 nC
C_{gs}	Gate to source capacitance	1.1 nF

The main parameter specifications of the GaN SPA are listed in Table I, and the main parameter specifications of the GaN HEMT are listed in Table II. The GaN SPA is applied in a 500 kW MS FESS prototype. The MS FESS prototype is presented in Fig. 16. The MS FESS prototype has a 58-kg carbon fiber flywheel rotor. The flywheel rotor is braced by the AMBs, which can achieve a high rotation speed without friction. The main specifications of the MS FESS are listed in Table III. The main parameters of the AMB in the MS FESS are listed in Table IV. The Rohde & Schwarz FSH4 spectrum analyzer, HIOKI PW6001 power analyzer, HIOKI CT6700 high accuracy current sensor, FLIR OnePro thermal imager, and Tektronix oscilloscope are

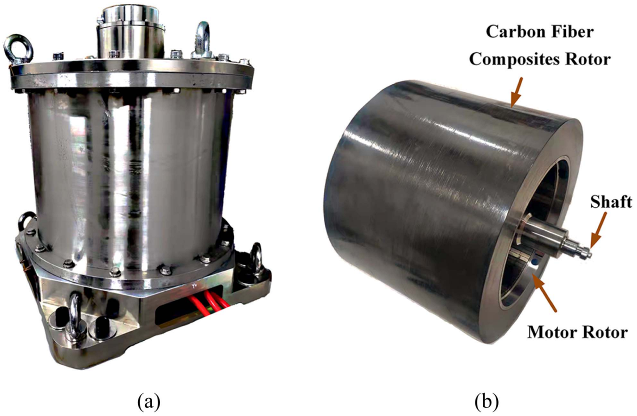

(a) (b)

Fig. 16. (a) FESS prototype. (b) Carbon fiber composites flywheel rotor of the FESS prototype.

TABLE III
MAIN PARAMETER SPECIFICATIONS OF THE FESS

Symbol	Description	Value
V_{DC}	Maximum voltage	500 V
P_r	Maximum power	500 kW
E_m	Stored energy	1.2 kWh
ω_m	Maximum design Speed	27000 r/min
Mr	Rotor weight	58.0 kg
S_m	Prototype Size	Φ500×590 mm

TABLE IV
MAIN PARAMETER SPECIFICATIONS OF THE AMBS IN THE FESS

Symbol	Description	Value
k_{ia}	Current stiffness of axial AMB	140 N/A
k_{xa}	Position stiffness axial AMB	1.25 MN/m
k_{ir}	Current stiffness of radial AMB	165 N/A
k_{ir}	Position stiffness radial AMB	5.00 MN/m
L_a	Inductance of axial AMB	5.5 Ω
R_a	Resistance of axial AMB	4.2 mH
L_r	Inductance of radial AMB	6.2 Ω
R_r	Resistance of radial AMB	4.8 mH

used to measure the bandwidth, current ripple, efficiency, and temperature of the GaN SPA.

B. Experiment 1: Switching Time

The theoretical dead time can be calculated according to (13) and (14). To verify the theoretical dead time can be effectively applied to GaN SPA, the experiment of the switching time is performed.

According to Fig. 3, the gate driver circuit of the GaN SPA needs a suitable turn-ON and turn-OFF resistor. Thus, the determination of the turn-ON and turn-OFF resistors is first analyzed. The output voltages of the different turn-ON and turn-OFF resistors are shown in Fig. 17. From Fig. 17, a small turn-ON and turn-OFF resistor will cause a switching oscillation, and a large turn-ON and turn-OFF resistor will cause a long turn-ON and turn-OFF time. Based on Fig. 17, the turn-ON and turn-OFF resistors 18 and 15 Ω are used in this article.

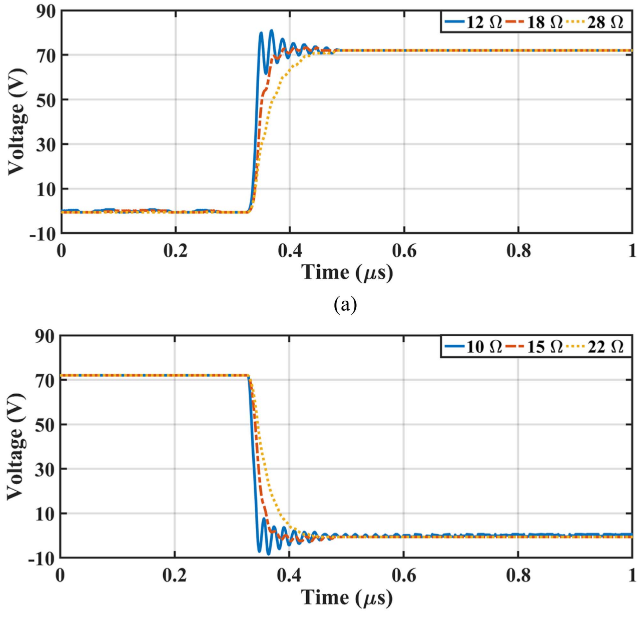

(a)

(b)

Fig. 17. (a) Output voltage of different turn-ON resistors. (b) Output voltage of different turn-off resistors.

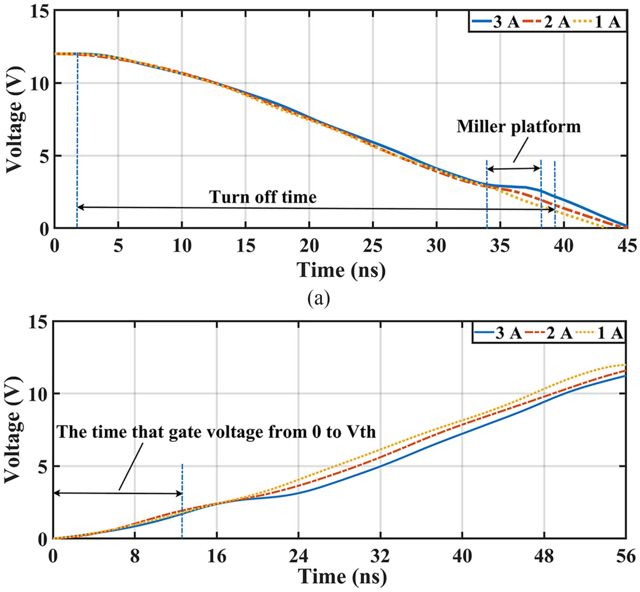

(a)

(b)

Fig. 18. Tested gate voltage of different load currents. (a) Turn-OFF process. (b) Turn-ON process.

The switching time is varied with the load current. Thus, the gate voltage of different load currents is tested. The gate voltage is shown in Fig. 18. According to Fig. 18, the switching time increases when the load current increases. Thus, the dead time of the GaN SPA should be adjusted according to the load current. The theoretical dead time and the tested minimum dead time are listed in Table V. The theoretical optimal dead is close to the tested minimum OTD, and the error is smaller than 8.9%.

TABLE V
THEORETICAL OTD AND THE OTD

Load current	Theoretical dead time	Theoretical dead time with the margin	Tested optimal dead time
1 A	23.9 ns	33.1 ns	22.1 ns
2 A	25.6 ns	35.8 ns	23.5 ns
3 A	27.2 ns	38.1 ns	26.2 ns

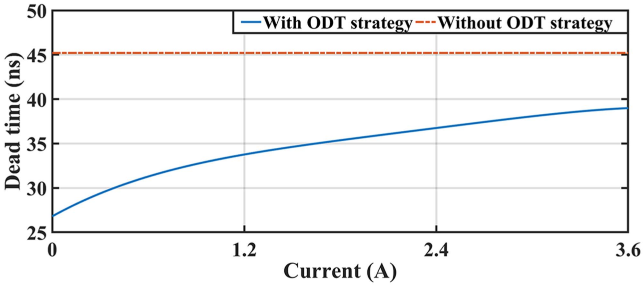

Fig. 19. Dead time with and without ODT strategy.

The practical dead time is set as 1.4 times the theoretical dead time in this article. Without an ODT strategy, the dead time is usually set as the turn-off time of the switching device. The applied dead time with and without the ODT strategy is shown in Fig. 19. The dead time with the ODT strategy can be reduced. The experimental results illustrate that the theoretical dead time with the margin can be efficiently applied to the GaN SPA to reduce the dead time. Such that the reverse conduction loss can be reduced.

C. Experiment 2: Bandwidth and Current Ripple

To verify that the GaN SPA can achieve a wide bandwidth and low current ripple, the bandwidth and the step response curve are measured. Furthermore, an experimental comparison with the conventional Si MOSFET SPA and SiC MOSFET SPA is presented. A PI controller is used for the current control. The FSH4 spectrum analyzer is used to analyze the current bandwidth. The CT6700 current sensor is used to measure the current ripple.

The GaN SPA operates at a switching frequency of 120 kHz. Fig. 20(a) shows the current step response versus the dc-link voltage. When the dc-link voltage increases, the response speed and the current ripple increase. With the high switching frequency, the current ripple can be smaller than 28 mA at the dc-link voltage of 72 V. Fig. 20(b) shows the Bode plots of the GaN SPA. As the dc-link voltage increases, the SPA can obtain a wider bandwidth. The bandwidth can be larger than 1268 Hz with a dc-link voltage of 72 V.

The Si MOSFET SPA operates at a switching frequency of 20 kHz, and the SiC MOSFET SPA operates at a switching frequency of 40 kHz. The step response curve and Bode plot of the SiC MOSFET SPA and Si MOSFET SPA are presented in Figs. 21 and 22, respectively. The comparisons of the GaN SPA, Si MOSFET SPA, and SiC MOSFET SPA are listed in Table VI. At the same current ripple, the GaN SPA has a wider current bandwidth. In the same current bandwidth, the GaN SPA has a lower current ripple. The experimental results illustrate that the proposed GaN SPA has a better performance on the current bandwidth and current ripple.

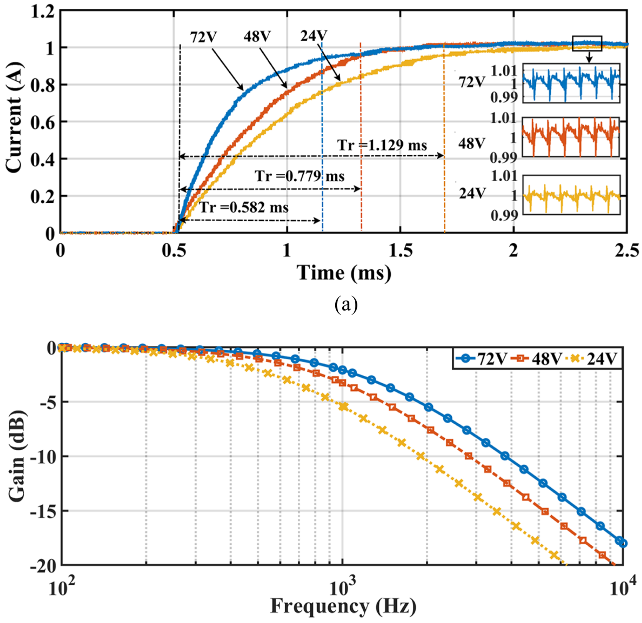

(a)

(b)

Fig. 20. Current step response curve and Bode plot of the GaN SPA. (a) Step response curve. (b) Bode plot.

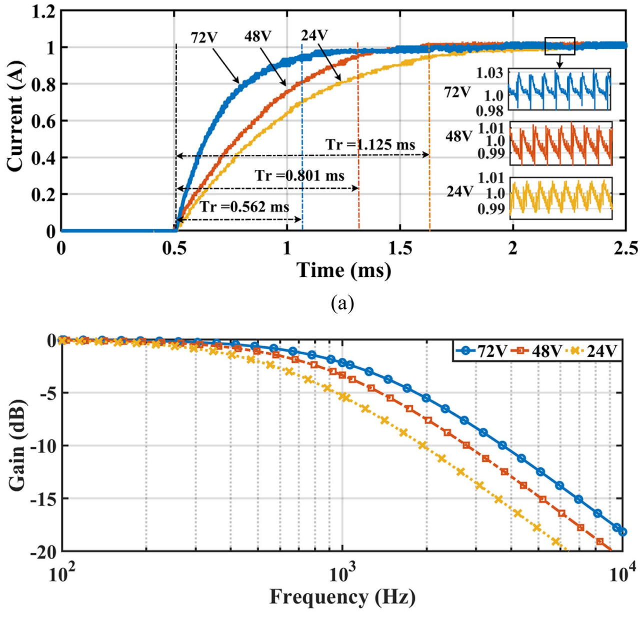

(a)

(b)

Fig. 21. Current step response curve and Bode plot of the SiC MOSFET SPA. (a) Step response curve. (b) Bode plot.

D. Experiment 3: Efficiency of the GaN SPA

To verify that the low-loss PWM method and ODT strategy can improve efficiency, the efficiency of the SPA is measured by a power analyzer. Furthermore, an experimental comparison with

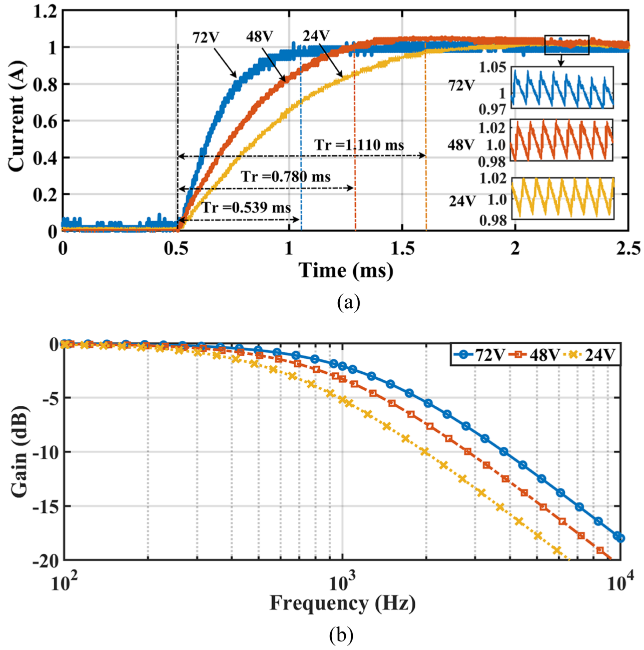

Fig. 22. Current step response curve and Bode plot of the Si MOSFET SPA. (a) Step response curve. (b) Bode plot.

TABLE VI
BANDWIDTH AND CURRENT RIPPLE OF THE SPAS

Types of SPAs	DC-link voltage	Bandwidth	Response time	Current ripple
GaN HEMTS SPA @ 120 kHz	24 V	635 Hz	1.129 ms	13 mA
	48 V	942 Hz	0.779 ms	19 mA
	72 V	1268 Hz	0.582 ms	28 mA
SiC MOSFET SPA @ 40 kHz	24 V	646 Hz	1.125 ms	26 mA
	48 V	927 Hz	0.801 ms	35 mA
	72 V	1245 Hz	0.562 ms	47 mA
Si MOSFET SPA @ 20 kHz	24 V	660 Hz	1.110 ms	34 mA
	48 V	943 Hz	0.780 ms	51 mA
	72 V	1272 Hz	0.539 ms	78 mA

the conventional two-level PWM method [15] and three-level PWM method [20] is performed.

Fig. 23(a) shows the power consumption of the GaN SPA versus current. Fig. 23(b) shows the efficiency of the GaN SPA versus current. The two-level PWM method requires a diode freewheeling state. However, the GaN HEMT does not have an antiparallel diode. It can only operate at a diode-like character, which results in a larger voltage drop. Thus, the two-level PWM method will have poor performance with respect to efficiency. Compared to the three-level PWM method, the low-loss PWM method can reduce the switching times; thus, the efficiency of the low-loss PWM method is increased. The loss of the SPA can be further reduced by adopting the ODT strategy. The efficiency of the GaN SPA with the low-loss PWM method and ODT strategy can be larger than 85.7%, which is increased by 5.2% compared to the conventional three-level PWM method. The experimental results illustrate that the proposed low-loss PWM method with the ODT strategy can increase the efficiency of the GaN SPA.

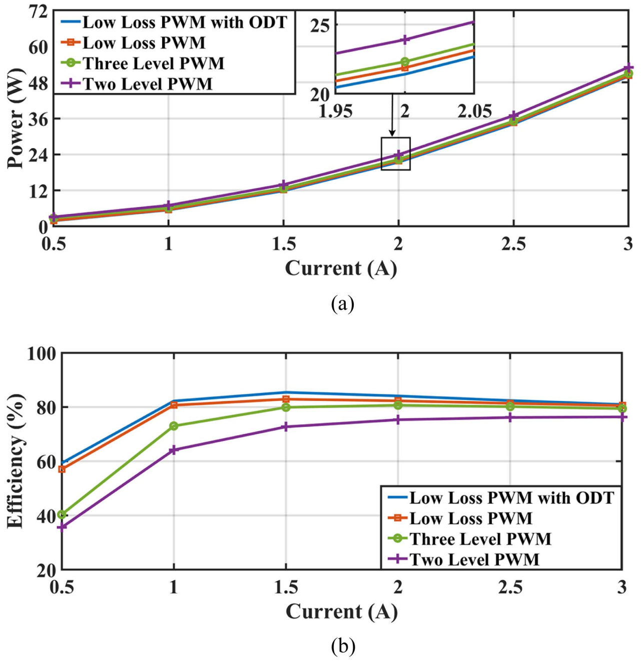

Fig. 23. (a) Power consumption versus current of one channel. (b) Efficiency versus currents of one channel.

The loss of the GaN SPA will convert to heat, which will cause a temperature rise. The temperature of the GaN SPA is measured in this article. The GaN HEMT XG65T125HS1B adopts a dual-flat no-leads (DFN) package, which has fine heat dissipation capacity. The thermal resistance of junction-to-case of XG65T125HS1B is 1.85 °C/W, and the thermal resistance of junction-to-ambient is 50.0 °C/W. The ambient temperature of the laboratory is 24 °C. A 12-layer printed circuit board (PCB) is adopted to achieve satisfactory heat dissipation. The average thermal conductivity of the PCB is 16.3 W/(mK). When the output current is a sinusoidal current with an amplitude of 3 A, the temperature rise of different PWM methods is shown in Fig. 24. With the proposed low-loss PWM method, Q_{n2} and Q_{n4} have a longer operating time than Q_{n1} and Q_{n3}. Thus, the temperature of Q_{n2} and Q_{n4} is higher than Q_{n1} and Q_{n3}. When the low-loss PWM method with the ODT strategy is used, the GaN SPA has the highest efficiency. Thus, the temperature rise of the low-loss PWM method with the ODT strategy is the lowest, and the temperature of the GaN HEMT is lower than 34.7 °C. The two-level PWM method has the lowest efficiency. Thus, the temperature rise of the two-level PWM method is the highest. The temperature rises influence the transconductance of the GaN SPA, which will cause an error in the switching model. Nevertheless, the temperature rise of the GaN SPA is relatively low. Therefore, the influence of the temperature on transconductance does not consider, and the transconductance at the temperature of 25 °C is adopted to calculate the dead time in this article. The experimental results illustrate that the proposed low-loss PWM method with the ODT strategy can reduce the temperature rise of the GaN SPA.

The gate driver power consumption is also related to the PWM method. The gate driver power consumption can be reduced by

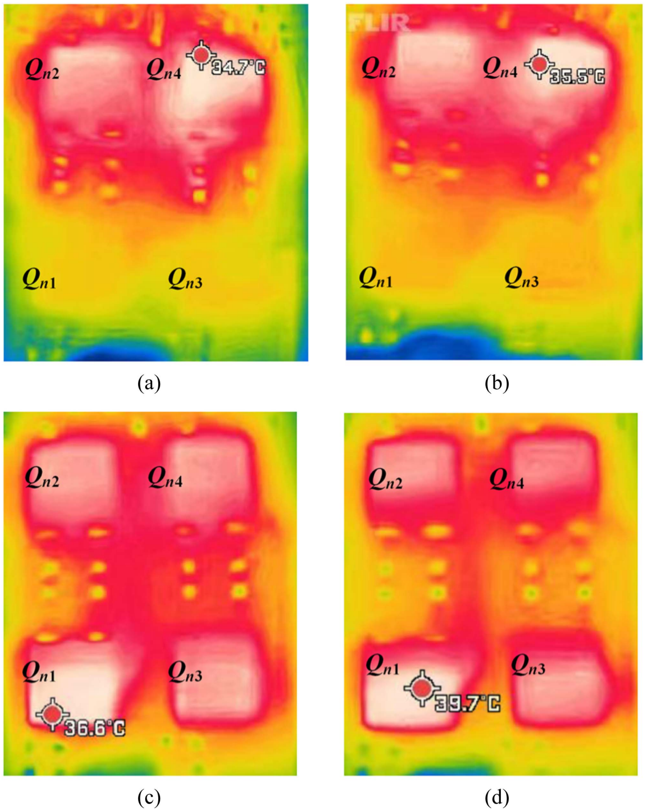

(a) (b) (c) (d)

Fig. 24. Temperature of the GaN SPA of different PWM methods. (a) Low-loss PWM method with ODT. (b) Low loss PWM method. (c) Three-level PWM method. (d) Two-level PWM method.

TABLE VII
POWER CONSUMPTION OF THE IRS2110 GATE DRIVER OF DIFFERENT PWM METHODS

PWM methods	Power consumption
low-loss PWM method	0.556 W
Three-level PWM method	0.592 W
Two-level PWM method	0.530 W

reducing the switching times. The power consumption of the gate drive circuit in Fig. 3 is measured. An H-bridge required two IRS2110 gate drivers. The power consumptions of the IRS2110 gate drivers in one H-bridge are listed in Table VII. The switching times of the low-loss PWM method are half of the three-level method. Thus, the power consumption of the low-loss PWM method is smaller than the three-level PWM method. The two-level PWM method has the minimum switching times among the three PWM methods. Thus, the gate driver power consumption of the two-level PWM method is minimal. However, the two-level PWM method will cause a large reverse conduction loss. The gate driver power consumption is relatively tiny compared to the power of the GaN HEMT. However, considering the power consumption of the gate driver is also significant, such as in the power supply design of the gate driver IC.

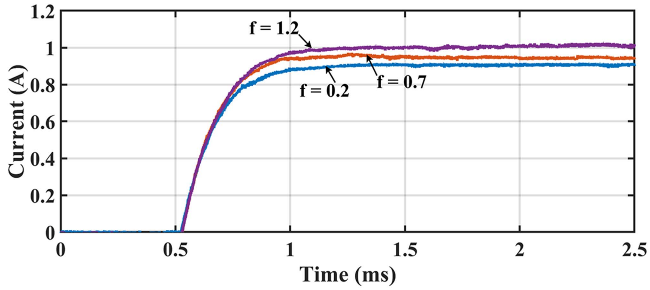

Fig. 25. Step response curves of the DBMPCC versus the feedback correction coefficient.

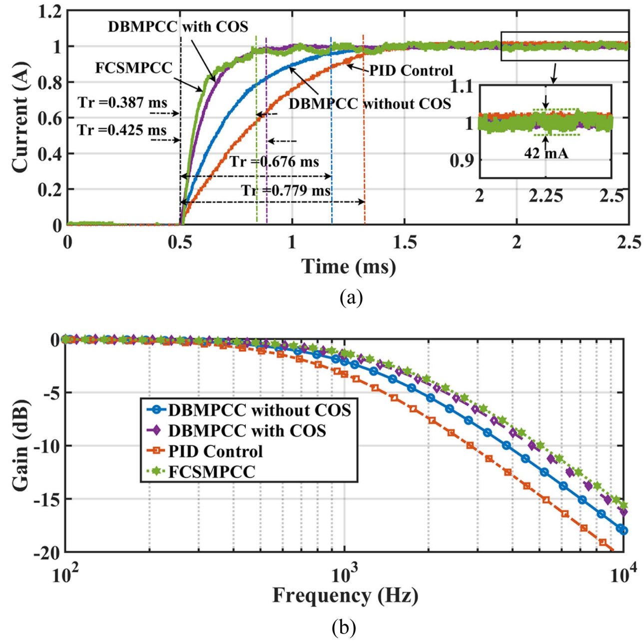

(a)

(b)

Fig. 26. Current step response curve and Bode plot of DBMPCC without COS, DBMPCC with COS, PID control, and FCSMPCC under 48 V. (a) Step response curve. (b) Bode plot.

E. Experiment 4: Applied DBMPCC to the GaN SPA

The proposed DBMPCC without and with COS are implemented in the GaN SPA to increase the bandwidth. The PID control is the most commonly used in the SPA. The FCSMPCC has been applied to the SPA in recent years [26]. Thus, DBMPCC is compared with the conventional PID control and FCSMPCC. The comparison is under the dc-link voltage of 48 and 72 V.

The DBMPCC requires a feedback correction coefficient to obtain a satisfying control accuracy. The feedback correction coefficient is adjusted according to experimental control accuracy in this article. The step response curve versus the feedback correction coefficient is shown in Fig. 25. From Fig. 25, the control accuracy can be improved by increasing the feedback correction coefficient. When the feedback correction coefficient is 1.2, the steady-state error can be smaller than 2%. Thus, in this article, the feedback correction coefficient is 1.2.

Fig. 26 shows the current step response curves and Bode plots of DBMPCC, PID control, and FCSMPCC with the dc-link

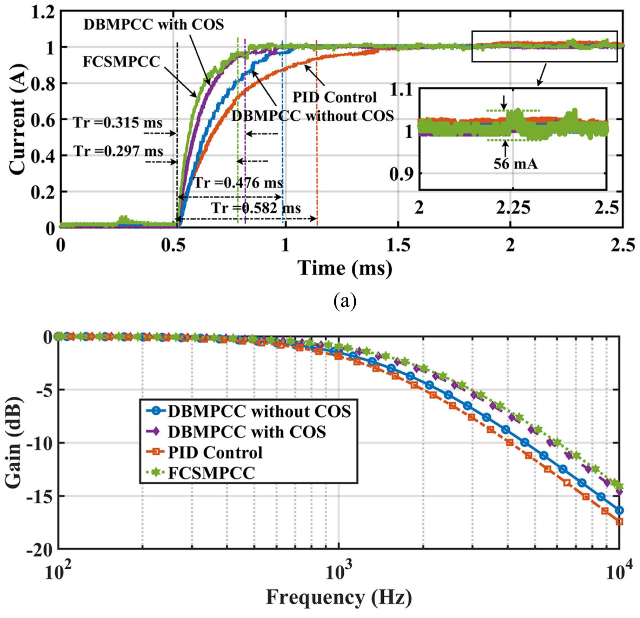

(a)

(b)

Fig. 27. Current step response curves and Bode plots of DBMPCC without COS, DBMPCC with COS, PID control, and FCSMPCC under 72 V. (a) Step response curve. (b) Bode plot.

TABLE VIII
BANDWIDTH AND CURRENT RIPPLE OF THE CONTROL METHODS

DC-link voltage	Control methods	Bandwidth	Response time	Current ripple
48 V	PID Control	942 Hz	0.779 ms	19 mA
	DBMPCC without COS	1102 Hz	0.676 ms	19 mA
	DBMPCC with COS	1568 Hz	0.425 ms	20 mA
	FCSMPCC	1683 Hz	0.387 ms	42 mA
72 V	PID Control	1272 Hz	0.582 ms	28 mA
	DBMPCC without COS	1447 Hz	0.476 ms	28 mA
	DBMPCC with COS	1893 Hz	0.315 ms	28 mA
	FCSMPCC	2011 Hz	0.297 ms	56 mA

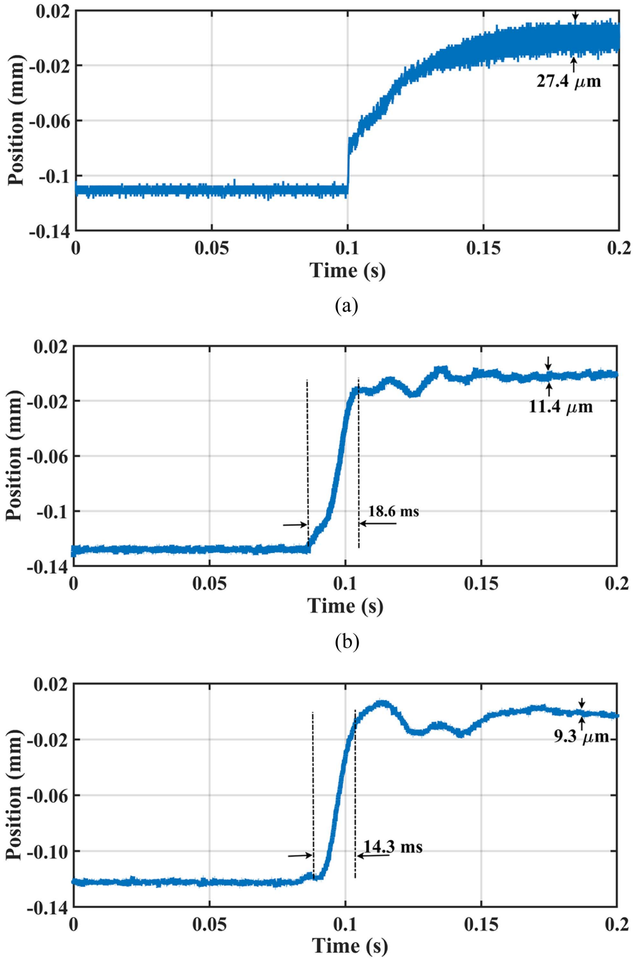

(a)

(b)

(c)

Fig. 28. Position response curve of the *x-axis.* (a) Si MOSFET SPA with dc-link voltage of 72 V. (b) Si MOSFET with dc-link voltage of 48 V. (c) GaN SPA with dc-link voltage of 72 V.

voltage of 48 V. Compared to the PID control, the DBMPCC with and without COS has a faster current response and wider current bandwidth. The DBMPCC without COS will cause the control output to be reduced. Thus, the DBMPCC with COS has a faster current response than that without COS. Among these methods, the FCSMPCC has the fastest current response speed and widest current bandwidth. However, the FCSMPCC only can apply one switching state in one control period and has no fixed switching frequency. Thus, the FCSMPCC has the largest current ripple of 42 mA.

Fig. 27 shows the current step response curves and Bode plots of DBMPCC, PID control, and FCSMPCC with the dc-link voltage of 72 V. Similar to the condition of dc-link voltage 48 V, DBMPCC has a faster response speed than the PID control. The FCSMPCC has the fastest response speed and largest current ripple. A comprehensive comparison of the control methods is listed in Table VIII. According to Table VIII, the current bandwidth can be increased by increasing the dc-link voltage in the same control methods. Compared to the conventional PID control, the current bandwidth can increase by 621 Hz and 48.8% by using DBMPCC with COS.

F. Experiment 5: Applied GaN SPA to 5-DOF Control

The GaN SPA is applied in the 5-DOF MS control. The comparison of control performance with the Si MOSFET SPA is presented. When Si MOSFET SPA with 72 V is used, the *x-axis* position response curve is shown in Fig. 28(a). In Fig. 28(a), the rotor has violent vibration because the Si MOSFET SPA has a considerable current ripple. (The analysis of the relationship between current ripple and vibration is presented in Appendix II.) From Table VI, the MOSFET SPA with 72 V has a current bandwidth of 1271 Hz. However, considering the vibration in the rotor, the Si MOSFET SPA cannot achieve this current bandwidth. When the dc-link of the Si MOSFET SPA reduces to 48 V, the position response curve is shown in Fig. 28(b), and the vibration can be suppressed. The position response curve of the GaN SPA with 72 V is shown in Fig. 28(c). Because the GaN SPA with a high switching frequency can have a low current ripple, the vibration does not occur. From Table VI, the GaN SPA with 72

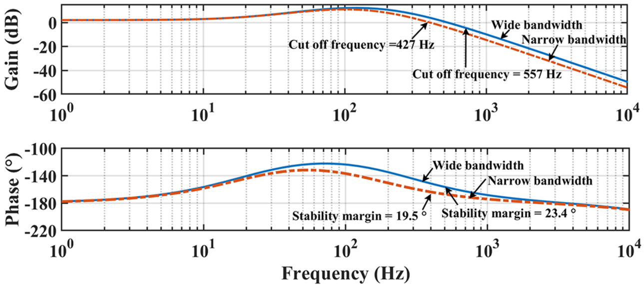

Fig. 29. Bode plot of the open-loop system of position control with wide bandwidth and narrow bandwidth SPA.

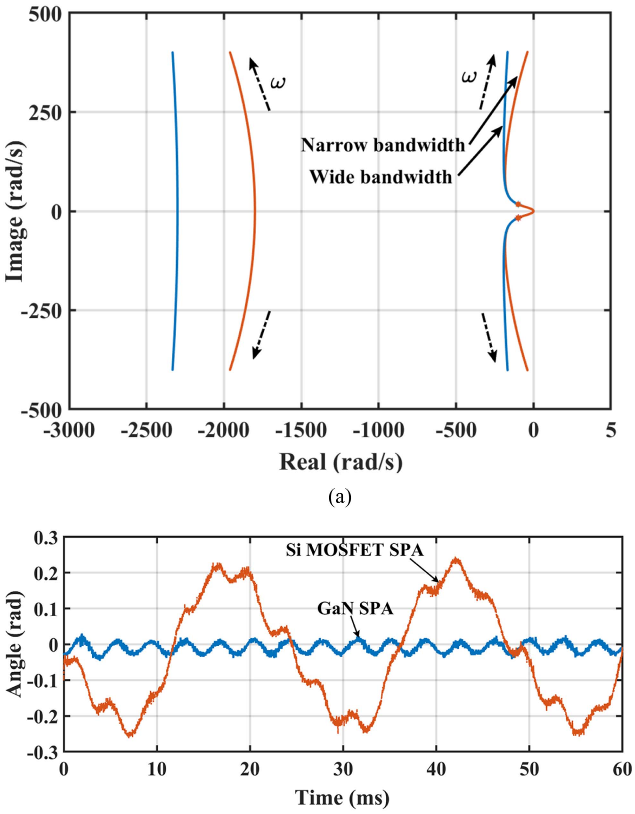

(a)

(b)

Fig. 30. (a) Root locus of the rotation speed with wide bandwidth and narrow bandwidth SPA. (b) Rotation angle α of the flywheel rotor.

V shows a wider bandwidth and low current ripple than the Si MOSFET SPA with 48 V. Thus, the MS with the GaN SPA shows higher position control accuracy and faster position response speed, as shown in Fig. 28(b) and (c).

The comparison of the GaN SPA and Si MOSFET SPA is further performed in the frequency domain. The GaN SPA shows a wider bandwidth than the Si MOSFET SPA. The bode plot of the open-loop transfer function with SPA of wide and narrow bandwidth is shown in Fig. 29. According to Fig. 29, the control system with SPA of a wider bandwidth can have a larger stability margin. Additionally, the control system with the SPA of wider bandwidth has a larger cut-off frequency and fast response speed. However, the gain of the Bode plot with SPA of wider bandwidth has a larger peak value. According to the theory of frequency-domain analysis, the larger peak in the bode plot will cause a larger overshoot [43]. As shown in Fig. 28(b) and (c), the overshoot of the position control with GaN SPA is slightly large than with the Si MOSFET SPA.

Additionally, a wide current bandwidth can enhance the stability of the MS control and overcome the whirl motion. The root locus of the rotation speed of different current bandwidths is presented in Fig. 30(a). With a wider bandwidth, the root locus moves left. The stability margin can be increased. The rotation angle α of GaN SPA and Si MOSFET SPA is shown in Fig. 30(b). At the speed of 16 000 r/min, the MS control system occurs a whirling motion using the Si MOSFET SPA. The whirling motion can be suppressed with the GaN SPA. The experimental result illustrates that the proposed GaN SPA can enhance the stability of the MS control system of the FESS. (The analysis of the relationship between current bandwidth and rotor stability is presented in Appendix I.)

VI. CONCLUSION

In this article, a new GaN SPA is proposed for the AMB of a FESS to achieve a wide bandwidth and low current ripple. The main conclusions are drawn as follows.

1) Compared to the Si MOSFET SPA and SiC MOSFET SPA, the GaN SPA has a wider current bandwidth in the same current ripple condition and shows a lower current ripple at the same current bandwidth. The GaN SPA can achieve a bandwidth of 1268 Hz and a current ripple of 28 mA.
2) With the proposed low-loss PWM method and ODT strategy, the GaN SPA has a higher efficiency. Compared to the conventional two-level PWM method [15] and three-level PWM methods [20], the maximum efficiency of the GaN SPA with the low-loss PWM method and ODT strategy increases by 8.3% and 5.2%, respectively.
3) The proposed DBMPCC is implemented in the GaN SPA to broaden the current bandwidth. Compared to the PID control, the bandwidth of the DBMPCC is increased by 621 Hz and 48.8%.
4) The proposed GaN SPA is implemented in the 5-DOF MS control of the FESS. The experimental results show that the GaN SPA can achieve higher control accuracy and enhance the stability of the MS control system compared to the Si MOSFET SPA.

APPENDIX I

In Appendix I, the influence of the bandwidth of the PA on the stability of the magnetic suspended system is discussed. The 5-DOF MS control includes position control and rotation control. The stability of the position control is analyzed through the frequency-domain analysis method. The model of the position control is presented as

$$G_p(s) = \frac{k_i}{M_r s^2 - k_x} \tag{1a}$$

where k_i is the current stiffness, k_x is the position stiffness, and M_r is the rotor mass.

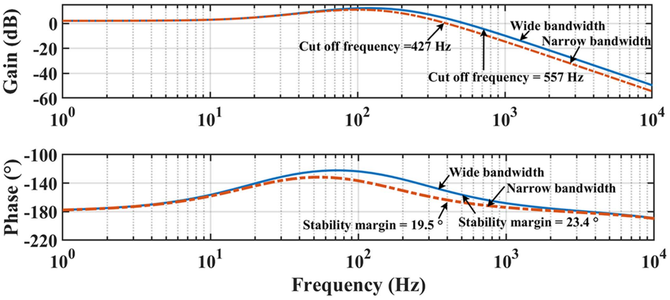

Fig. 31. Bode plot of the open-loop system of position control with wide bandwidth and narrow bandwidth SPA.

The position control adopts a PD controller. The model of the PD controller is presented as

$$C_p(s) = \frac{k_p + k_d s}{T_c s + 1} \tag{2a}$$

where k_p is the proportional coefficient, k_d is the differential proportional coefficient, and T_c is the filter coefficient of the PD controller.

The SPA can be regarded as a first-order inertial element, presented as

$$G_p = \frac{1}{T_p s + 1} \tag{3a}$$

where T_p is the time constant of the SPA.

The open-loop transfer function can be deduced as

$$G_o(s) = \frac{k_i (k_p + k_d s)}{(ms^2 - k_x)(T_p s + 1)(T_c s + 1)}. \tag{4a}$$

The Bode plot of the open-loop transfer function with SPA of wide and narrow bandwidth is shown in Fig. 31. According to Fig. 31, the control system with SPA of a wider bandwidth can have a more considerable stability margin. Additionally, the control system with the SPA of wider bandwidth has a larger cut-off frequency and fast response speed.

The stability of the rotation control is analyzed through the root locus method. The model of the rotation control is presented as

$$\begin{cases} J_d \frac{d\alpha}{dt^2} - J_p \omega \frac{d\beta}{dt} - k_{ra}\alpha = M_\alpha \\ J_d \frac{d\beta}{dt^2} + J_p \omega \frac{d\alpha}{dt} - k_{ra}\beta = M_\beta \end{cases} \tag{5a}$$

where J_d is the polar moment inertia, J_p is the equatorial moment inertia, k_{rq} is angular displacement stiffness, and M_α and M_β are moments of force.

The moment of forces can be deduced as

$$\begin{cases} M_\alpha = k_{ri} i_\alpha = k_{ri} i_{\alpha r} - k_{ri} T_p \frac{di_\alpha}{dt} \\ M_\beta = k_{ri} i_\beta = k_{ri} i_{\alpha r} - k_{ri} T_p \frac{di_\beta}{dt} \end{cases} \tag{6a}$$

where k_{ri} is the current stiffness coefficient of rotation.

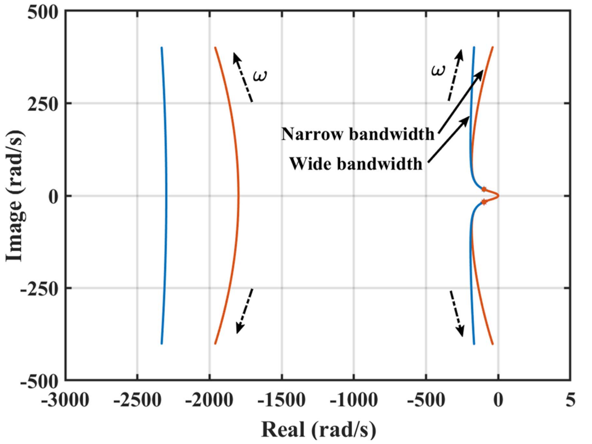

Fig. 32. Root locus of the rotation speed with wide bandwidth and narrow bandwidth SPA.

The rotation control also adopts a PD controller, which is presented as

$$\begin{cases} i_{\alpha r} = k_{rp}(\alpha_r - \alpha) + k_{rd}\frac{d(\alpha_r - \alpha)}{dt} \\ i_{\beta r} = k_{ra}(\beta_r - \beta) + k_{rd}\frac{d(\beta_r - \beta)}{dt} \end{cases} \tag{7a}$$

where k_{rp} is the proportional coefficient and k_{rd} is the differential proportional coefficient of the rotation control.

Combining (5a), (6a), and (7a), the differential equation of the closed-loop system of rotation control is deduced as

$$\begin{cases} \frac{d^3\alpha}{dt^3} + p_2 \frac{d^2\alpha}{dt^2} + p_1 \frac{d\alpha}{dt^3} - p_{c1}\frac{d\beta}{dt} - p_{c2}\frac{d^2\beta}{dt^2} + p_0\alpha = q_\alpha \\ \frac{d^3\beta}{dt^3} + p_2 \frac{d^2\beta}{dt^2} + p_1 \frac{d\beta}{dt} + p_{c1}\frac{d\beta}{dt} + p_{c2}\frac{d^2\beta}{dt^2} + p_0\beta = q_\beta \end{cases} \tag{8a}$$

where

$$p_0 = \frac{(k_{rp}k_{ri} - k_a)}{T_p J_d}, p_1 = \frac{(k_{rd}k_{ri} + T_p k_a)}{T_p J_d}, p_2 = T_p$$

$$p_{c1} = \frac{J_p \omega}{T_p J_d}, p_{c2} = \frac{J_p \omega}{J_d}$$

$$q_\alpha = \frac{k_{rp}k_{ri}\alpha_r}{T_p J_d} + \frac{k_{rd}k_{ri}}{T_p J_d}\frac{d\alpha_r}{dt}, q_\beta = \frac{k_{rp}k_{ri}\beta_r}{T_p J_d} + \frac{k_{rd}k_{ri}}{T_p J_d}\frac{d\beta_r}{dt}.$$

The state matrix of the differential equation of (8a) can be deduced as

$$A = \begin{bmatrix} 0 & 1 & 0 & 0 & 0 & 0 \\ 0 & 0 & 1 & 0 & 0 & 0 \\ -p_0 & -p_1 & -p_2 & 0 & -p_{c1} & -p_{c2} \\ 0 & 0 & 0 & 0 & 1 & 0 \\ 0 & 0 & 0 & 0 & 0 & 1 \\ 0 & p_{c1} & p_{c2} & -p_0 & -p_1 & -p_2 \end{bmatrix}. \tag{9a}$$

Based on the state matrix of (9a), the root locus of the rotation speed of different current bandwidths can be obtained, which is presented in Fig. 32. With a wider bandwidth, the root locus moves left. The stability margin can be increased.

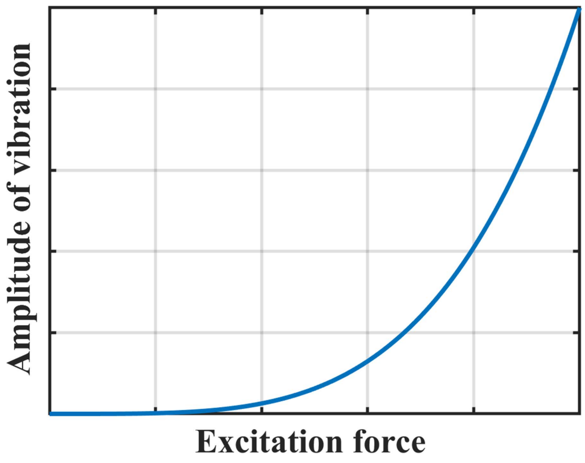

Fig. 33. Relationship between the vibration amplitude and excitation force.

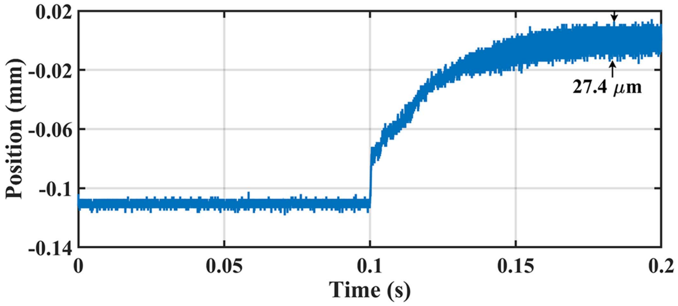

Fig. 34. Rotor vibration occurs when the current ripple is larger than 78 mA.

APPENDIX II

In Appendix II, the influence of the current ripple on rotor vibration is analyzed. The relationship between the magnetic force and current is can be deduced as[1]

$$f_{\text{mag}} = k_x x + k_i i_c \tag{10a}$$

where f_{mag} is the magnetic force.

According to (10a), the magnetic force is proportional to the current. Thus, the current ripple will cause a force ripple. The vibration model of the AMB control system is nonlinear, which can be deduced as [44]

$$\begin{aligned}&\ddot{x} + 2\mu b\dot{x} + b^2 x - \left(a_1 x^3 + a_2 x y^2 + a_3 x^2 \dot{x} + a_4 \dot{x} y^2\right.\\&\quad\left. + a_5 x \dot{y}^2 + a_6 x\dot{x} + a_7 x y \dot{y}\right) = F\cos\omega t\\&\ddot{y} + 2\mu b\dot{y} + b^2 y - \left(a_1 y^3 + a_2 y x^2 + a_3 y^2 \dot{y} + a_4 \dot{y} x^2\right.\\&\quad\left. + a_5 y \dot{x}^2 + a_6 y\dot{y}^2 + a_7 y x \dot{x}\right) = F\sin\omega t\end{aligned} \tag{11a}$$

where μ, a, and b are coefficients of the system, F is the excitation force, and ω is the angular frequency.

According to (11a), the relationship between the vibration amplitude and excitation force is shown in Fig. 33 [44]. According to Fig. 33, a large vibration amplitude will increase fast when the excitation force is larger than a certain value. In this article, the current ripple of the Si MOSFET SPA with a voltage of 72 V is larger than 78 mA, which will cause a relatively large force ripple. The magnetic suspend system with this SPA will have a significant vibration, as shown in Fig. 34.

REFERENCES

[1] H. Wang, Z. Wu, K. Liu, J. Wei, and H. Hu, "Modeling and control strategies of a novel axial hybrid magnetic bearing for flywheel energy storage system," *IEEE/ASME Trans. Mechatronics*, to be published, doi: 10.1109/TMECH.2022.3145705.

[2] C.-Y. Ho, J. Wang, K. Hu, and C. Liaw, "Development and operation control of a switched-reluctance motor driven flywheel," *IEEE Trans. Power Electron.*, vol. 34, no. 1, pp. 526–537, Jan. 2019.

[3] W. Zhang, J. Wang, P. Zhu, and J. Yu, "A novel vehicle-mounted magnetic suspension flywheel battery with a virtual inertia spindle," *IEEE Trans. Ind. Electron*, vol. 69, no. 6, pp. 5973–5983, Jun. 2022.

[4] N. F. Ershad, R. T. Mehrjardi, and M. Ehsani, "High-performance 4WD electric powertrain with flywheel kinetic energy recovery," *IEEE Trans. Power Electron.*, vol. 36, no. 1, pp. 772–784, Jan. 2021.

[5] M. I. Masouleh and D. J. N. Limebeer, "Fuel minimization for a vehicle equipped with a flywheel and battery on a three-dimensional track," *IEEE Trans. Intell. Veh.*, vol. 2, no. 3, pp. 161–174, Sep. 2017.

[6] M. L. Pastor, L. G.-T. Rodriguez, and C. V. Velez, "Flywheels store to save: Improving railway efficiency with energy storage," *IEEE Electrific. Mag.*, vol. 1, no. 2, pp. 13–20, Feb. 2013.

[7] A. Hutchinson and D. T. Gladwin, "Optimisation of a wind power site through utilisation of flywheel energy storage technology," *Energy Rep.*, vol. 6, pp. 259–265, 2020.

[8] S. Adhikari, R. Karki, and P. Piya, "Recovery risk mitigation of wind integrated bulk power system with flywheel energy storage," *IEEE Trans. Power Syst.*, vol. 34, no. 5, pp. 3484–3493, Sep. 2019.

[9] S. Mukoyama et al., "Development of superconducting magnetic bearing for 300 kW flywheel energy storage system," *IEEE Trans. Appl. Supercond.*, vol. 27, no. 4, Jun. 2017, Art. no. 3600804.

[10] M. Ghanaatian and S. Lotfifard, "Control of flywheel energy storage systems in the presence of uncertainties," *IEEE Trans. Sustain. Energy*, vol. 10, no. 1, pp. 36–45, Jan. 2019.

[11] F. N. Werfel et al., "A compact HTS 5 kWh/250 kW flywheel energy storage system," *IEEE Trans. Appl. Supercond.*, vol. 17, no. 2, pp. 2138–2141, Jun. 2007.

[12] W. Gengji and W. Ping, "Rotor loss analysis of PMSM in flywheel energy storage system as uninterruptable power supply," *IEEE Trans. Appl. Supercond.*, vol. 26, no. 7, Oct. 2016, Art. no. 0609905.

[13] W. E. Bialke, J. I. Minow, and R. M. Meloy, "Correlations of space-charging environments with aerospace mechanism friction anomalies," *IEEE Trans. Plasma Sci.*, vol. 47, no. 8, pp. 3872–3876, Aug. 2019.

[14] A. S. Nagorny, N. V. Dravid, R. H. Jansen, and B. H. Kenny, "Design aspects of a high speed permanent magnet synchronous motor/generator for flywheel applications," in *Proc. IEEE Int. Conf. Electric Mach. Drives*, 2005, pp. 635–641.

[15] Z. Yu, L. Gong, and C. Zhu, "Duty ratio stability and average steady-state error of two-level current-mode wide-bandwidth switching power amplifiers," *IEEE Trans. Power Electron.*, vol. 35, no. 4, pp. 4094–4104, Apr. 2020.

[16] H. Zhang et al., "Harmonic current suppression for AMB system via the finite dimension repetitive controller," *IEEE Sensors J.*, vol. 22, no. 7, pp. 6995–7004, Apr. 2022.

[17] S. Carabelli, F. Maddaleno, and M. Muzzarelli, "High-efficiency linear power amplifier for active magnetic bearings," *IEEE Trans. Ind. Electron*, vol. 47, no. 1, pp. 17–24, Feb. 2000.

[18] Z. Changsheng and M. Zhiwei, "A PWM based switching power amplifier for active magnetic bearings," in *Proc. Int. Conf. Elect. Mach. Syst.*, 2005, pp. 1563–1568.

[19] Z. J. Zhao et al., "Simulation and experiment of power amplifier for magnetic bearings," *Adv. Mater. Res.*, vol. 998-999, pp. 476–480, 2014.

[20] C. Zhu, C. Yang, Z. Dan, and C. Liang, "A current-control mode three-level PWM switching power amplifier for active magnetic bearings," in *Proc. Int. Conf. Elect. Mach. Syst.*, 2008, pp. 2217–2220.

[21] G. Cao, H. Sun, G. Yang, and D. Jiang, "Active magnetic bearing amplifier design based on SiC devices," in *Proc. IEEE Workshop Wide Bandgap Power Devices Appl. Asia*, 2021, pp. 382–386.

[22] D. Yang, W. Xing, X. Gao, Z. Ma, and Y. Zhu, "An adaptive control for switching power amplifier of AMB," *IEEE Trans. Transp. Electrific.*, vol. 8, no. 2, pp. 2374–2383, Aug. 2022.

[23] Y. He, X. He, J. Ma, and Y. Fang, "Optimization research on a switching power amplifier and a current control strategy of active magnetic bearing," *IEEE Access*, vol. 8, pp. 34833–34841, 2020.

[24] Y. Ren and J. Fang, "Current-sensing resistor design to include current derivative in PWM H-bridge unipolar switching power amplifiers for magnetic bearings," *IEEE Trans. Ind. Electron.*, vol. 59, no. 12, pp. 4590–4600, Dec. 2012.

[25] L. Tarisciotti, L. Papini, C. Ahumada, and P. Bolognesi, "Predictive control for an active magnetic bearing system with sensorless position control," in *Proc. IEEE Energy Convers. Congr. Expo.*, 2021, pp. 3267–3274.

[26] C. Liu, J. Zhan, J. Wang, Y. Yang, and Z. Liu, "An improved one-cycle control algorithm for a five-phase six-leg switching power amplifier in active magnetic bearings," *IEEE Trans. Ind. Electron.*, vol. 69, no. 12, pp. 12564–12574, Dec. 2022, doi: 10.1109/TIE.2021.3130336.

[27] J. Millan, P. Godignon, X. Perpiñà, A. Pérez-Tomás, and J. Rebollo, "A survey of wide bandgap power semiconductor devices," *IEEE Trans. Power Electron.*, vol. 29, no. 5, pp. 2155–2163, May. 2014.

[28] M. Dong, H. Li, S. Yin, Y. Wu, and K. Y. See, "A postprocessing-technique-based switching loss estimation method for GaN fevices," *IEEE Trans. Power Electron.*, vol. 36, no. 7, pp. 8253–8266, Jul. 2021.

[29] Z. Qi et al., "An accurate datasheet-based full-characteristics analytical model of GaN HEMTs for deadtime optimization," *IEEE Trans. Power Electron.*, vol. 36, no. 7, pp. 7942–7955, Jul. 2021.

[30] M. Asad, A. K. Singha, and R. M. S. Rao, "Dead time optimization in a gan-based buck converter," *IEEE Trans. Power Electron.*, vol. 37, no. 3, pp. 2830–2844, Mar. 2022.

[31] T. LaBella, B. York, C. Hutchens, and J.-S. Lai, "Dead time optimization through loss analysis of an active-clamp flyback converter utilizing GaN devices," in *Proc. IEEE Energy Convers. Congr. Expo.*, 2012, pp. 3882–3889.

[32] L. Hoffmann, C. Gautier, S. Lefebvre, and F. Costa, "Optimization of the driver of GaN power transistors through measurement of their thermal behavior," *IEEE Trans. Power Electron.*, vol. 29, no. 5, pp. 2359–2366, May 2014.

[33] D. Gu, J. Xi, and L. He, "Digitally controlled gan-based MHz active clamp flyback converter with dynamic dead time optimisation for AC-DC adapter," *IET Power Electron.*, vol. 13, no. 16, pp. 3777–3786, 2020.

[34] L. Schirone, M. Macellari, and F. Pellitteri, "Predictive dead time controller for gan-based boost converters," *IET Power Electron.*, vol. 10, no. 4, pp. 421–428, 2016.

[35] G. Schweitzer and E. H. Maslen, *Magnetic Bearings: Theory, Design, and Application to Rotating Machinery*. Berlin, Germany: Springer, 2009.

[36] A. K. Singha, "A discrete-time framework for designing stable digital V2 controllers for the buck converter," *IEEE Trans. Power Electron.*, vol. 37, no. 12, pp. 14317–14327, Dec. 2022, doi: 10.1109/TPEL.2022.3193066.

[37] X. Zhou, L. Wang, Y. Gan, H. Luo, Y.-F. Liu, and P. C. Sen, "Accurate analysis and design of the circuit parameters of LLC DC-DC converter with synchronous rectification," *IEEE Trans. Power Electron.*, vol. 37, no. 12, pp. 15051–15065, Dec. 2022, doi: 10.1109/TPEL.2022.3194588.

[38] E. A. Jones, Z. Zhang, and F. Wang, "Analysis of the dv/dt transient of enhancement-mode GaN FETs," in *Proc. IEEE Appl. Power Electron. Conf. Expo.*, 2017, pp. 2692–2699.

[39] E. A. Jones, "Review and characterization of gallium nitride power devices," M.S. thesis, Graduate School, Univ. Tennessee, Knoxville, TN, USA, 2016.

[40] M. S. R. Saeed, W. Song, L. Huang, and B. Yu, "Double-vector-based finite control set model predictive control for five-phase PMSMs with high tracking accuracy and DC-link voltage utilization," *IEEE Trans. Power Electron.*, vol. 37, no. 12, pp. 15234–15244, Dec. 2022, doi: 10.1109/TPEL.2022.3188578.

[41] W. Hua, F. Chen, W. Huang, G. Zhang, W. Wang, and W. Xia, "Multivector-based model predictive control with geometric solution of a give-phase flux-switching permanent magnet motor," *IEEE Trans. Ind. Electron*, vol. 67, no. 12, pp. 10035–10045, Dec. 2020.

[42] J. Wang, Y. Tang, P. Lin, X. Liu, and J. Pou, "Deadbeat predictive current control for modular multilevel converters with enhanced steady-state performance and stability," *IEEE Trans. Power Electron.*, vol. 35, no. 7, pp. 6878–6894, Jul. 2020.

[43] G. F. Franklin et al., *Feedback Control of Dynamic Systems*. Upper Saddle River, NJ, USA: Prentice Hall, 2002.

[44] A. Heydari, M. Mirparizi, F. Shakeriaski, F. S. Samani, and M. Keshavarzi, "Nonlinear vibration analysis of a rotor supported by magnetic bearings using homotopy perturbation method," *Propulsion Power Res.*, vol. 6, no. 3, pp. 223–232, 2017.

Hong-Jin Hu received the B.S. degree in automation from the Shaanxi University of Science and Technology, Xi'an, China, in 2016, and the M.Sc. degree in control theory and control engineering from the Shenzhen University, Shenzhen, China, in 2019. He is currently working toward the Ph.D. degree in mechanics with the Sun Yat-Sen University, Shenzhen, China.

His research interests include the flywheel energy storage system, PMSM control, and magnetic bearings control.

Kun Liu received the B.S. and M.S. degrees in automation from the Beihang University, Beijing, China, in 1985 and 1988, respectively, and the Ph.D. degree in rocket engine from the National University of Defense Technology, Changsha, China, in 1999.

He is currently a Professor and a Ph.D. Candidate Supervisor with the School of Aeronautics and Astronautics, Sun Yat-sen University, Shenzhen, China. His current research interests include design and control of magnetically suspended flywheel and control moment gyroscope, magnetically suspended flywheel energy storage system, an inertially stabilized platform using magnetic bearings, and dynamics and control of flight vehicles.

Haoze Wang (Member, IEEE) received the B.S. degree in engineering mechanics and the M.S. and Ph.D. degrees in astronautical science and technology from the National University of Defense Technology, Changsha, China, in 2006, 2010, and 2015, respectively.

He is currently an Associate Research Fellow with the School of Aeronautics and Astronautics, Sun Yat-sen University, Shenzhen, China. He was involved in research on magnetically suspended flywheel energy storage, high-pulsed power technologies, and the design and control of magnetic bearing.

Jing-Bo Wei received the B.S. degree in space engineering and the M.S. and Ph.D. degrees in aeronautical and astronautical science and technology from the National University of Defense Technology, Changsha, China, in 2009, 2011, and 2016, respectively.

He is currently an Associate Professor with the School of Aeronautics and Astronautics, Sun Yat-sen University, Guangzhou, China. His research interests include aerospace electronic technology, magnetic bearing technology, and power electronic technology.